Oceanic internal wave amplitude retrieval from satellite images based on a data-driven transfer learning model

Wang, Xudong; Wang, Haoyu; Wang, Shuo; Liu, Yanliang; Yu, Weidong; Wang, Jing; Xu, Qing; Li, Xiaofeng

DOI:
10.1016/j.rse.2022.112940

Oceanic Internal wave amplitude retrieval from satellite images based on a data-driven transfer learning model

Xudong Zhang[a], Haoyu Wang[a], Shuo Wang[b], Yanliang Liu[c,d], Weidong Yu[e,f], Jing Wang[g], Qing Xu[g], Xiaofeng Li[a*]

[a] CAS Key Laboratory of Ocean Circulation and Waves, Institute of Oceanology, Chinese Academy of Sciences and Center for Ocean Mega-Science, Chinese Academy of Sciences. No.7 Nanhai Road, 266071 Qingdao, China

[b] School of Computer Science, University of Birmingham, UK

[c] Center for Ocean and Climate Research, First Institute of Oceanography, Ministry of Natural Resources, Qingdao, China

[d] Laboratory for Regional Oceanography and Numerical Modeling, Pilot National Laboratory for Marine Science and Technology (Qingdao), Qingdao, China.

[e] School of Atmospheric Sciences, Sun Yat-Sen University, Zhuhai, China

[f] Key Laboratory of Tropical Atmosphere-Ocean System (Sun Yat-Sen University), Ministry of Education, China

[g] Facult of Information Science and Engineering, Ocean University of China, China

Corresponding author: X. Li (lixf@qdio.ac.cn)

Highlights:

- Lab experiment and satellite-field measurements are used to build two IW datasets.

- A transfer-learning model was developed based on the datasets.
- The model can retrieve IW amplitudes from satellite images.
- The model's MRE can be expected to be 10% for an IW amplitude of 100 m.
- Application of the model in the Andaman Sea shows IW amplitude spatial variations.

Abstract

Internal waves (IW) are characterized by a large-amplitude, long-wave crest, and long-propagation distance. They are widespread in the global ocean. Amplitude is an essential IW parameter and is difficult to derive from the IW surface signatures in satellite images. A laboratory experiment and combined satellite/in-situ measurements were carried out to build two internal wave datasets (888 pairs of lab data and 121 pairs of synchronous in-situ data and satellite images). To efficiently use the lab data, we implemented a transfer learning model to retrieve IW amplitude from satellite images. The model is a purely data-driven model pre-trained with lab data and re-trained with satellite/in-situ data. A short connection was incorporated into the transfer learning framework to reduce information loss. Bias correction was adopted to improve the model performance. After the correction, the root mean square error (RMSE) of the estimated IW amplitude decreased from 12.09 m (17.84 m) to 9.59 m (11.59 m), the mean relative error decreased from 21% (27%) to 18% (16%), and the correlation coefficients improved from 0.81 (0.72) to 0.89 (0.90) on the test (training) dataset. For IWs with amplitude exceeding 100 m, the model can be expected to get an absolute error of 10 m. The mean relative error decreased with the increase in IW amplitudes. Comparisons with other algorithms demonstrate that the proposed model is efficient for IW studies. We applied the model to 156 satellite images containing IW signatures in the Andaman Sea, finding that large-amplitude IWs were mainly located at the water depth between 200 m and 1,000 m on the continental slope. When considering one-pixel input errors for the peak-to-peak (PP) distance, the

model shows large tolerance with the errors. Compared with the KdV equation-based method, the developed model was more accurate.

Keywords: Internal wave, amplitude, transfer learning, remote sensing, in-situ measurement, laboratory experiment

1 Introduction

Internal waves (IW) are a ubiquitous phenomenon in the global ocean (Apel et al., 1985; Guo et al., 2012; Kozlov et al., 2014; Lavrova and Mityagina, 2017; Lindsey et al., 2018; Liu et al., 1998; Osborne and Burch, 1980; Scotti et al., 2008; Zhang et al., 2020; Zhao et al., 2014; Xu et al., 2008). IWs are characterized by their large amplitudes and long wave crests compared with surface waves. Field observations have shown that IW amplitudes range from tens of meters to hundreds of meters. For example, IW amplitude in the South China Sea reaches over 240 m (Huang et al., 2016). Large-amplitude IWs can propagate over several hundred kilometers before dissipating on the continental shelf. As a result, they cause sizeable vertical motion and strong shear forces of ocean currents, threatening marine navigation, transportation, and oil rig operation safety and affecting ocean environments, such as sediment resuspension and ocean mixing. Therefore, the accurate inversion of IW amplitude is necessary for IW studies.

Field observation is one of the best ways to obtain amplitudes of IWs and has developed very fast in recent years (Alford et al., 2010; Chen et al., 2019). In addition, IW characteristics, ocean mixing, and interactions between IWs or between IW and mesoscale processes have been studied based on in-situ observations (Liu et al., 2004; Shroyer et al., 2011; Zhao et al., 2004). However, the in-situ dataset is usually small in number and collected at fixed locations. Thus, they mainly serve as an independent test dataset to validate satellite observations or numerical results.

Remote sensing has already shown its potential and advantages in studying IWs for decades (Alpers, 1985; da Silva et al., 2012; Guo et al., 2012; Li et al., 2013; Li et al., 2008; Liu and Hsu, 2004; Marghany, 1999; Magalhaes and da Silva, 2018; Serebryany et al., 2020; Zhang et al., 2021; Marghany, 2021). Satellite images, both acquired by active microwave sensors, such as synthetic aperture radar image (SAR image), or passive optical sensors, such as the Moderate Resolution Imaging Spectroradiometer image (MODIS image), have become an important data source for IW studies. The benefit of combining the high spatial resolution and day-night imaging capabilities of SAR and high temporal resolution and a wide swath of MODIS sensors has led researchers to gain valuable knowledge of IWs in the past two decades. The spatiotemporal distributions (Liu and Hsu, 2004; Zubkova and Kozlov, 2020), generation mechanism (Magalhaes et al., 2020), propagation characteristics (Bai et al., 2017; Liu et al., 2014; Tensubam et al., 2021), interactions (Magalhaes et al., 2021; Xue et al., 2014), automatic detections (Li et al., 2020; Marghany, 2018), and the forecast of IWs (Zhang and Li, 2021; Zhang et al., 2021) have been extensively studied using satellite images. IW-induced currents will modulate the sea surface and produce convergence and divergence regions. The signal received by SAR images will be enhanced/weakened in the convergence/divergence region by the Bragg backscatter mechanism (Alpers, 1985). Passive optical images show clear IW signatures due to the specular reflection mechanism in areas with sun glitter. So surface signatures related to IWs can be clearly observed from satellite images.

In the literature, retrieval of IW amplitudes from satellite images has been mainly based on the Korteweg-De Vries (KdV) equation and the IW half-width characteristic (Zheng et al., 2001). The KdV equation is a simple form to describe IWs in shallow oceans. Since it has an analytical solution, researchers have used it to gain first-order knowledge of IW. However, in most cases, IW has far more complicated characteristics than those modeled using the KdV or extended KdV equations.

Machine learning techniques have recently shown their potential in oceanographic studies in various aspects (Li et al., 2020; Zheng et al., 2020), with different techniques proposed for different oceanic studies. Machine learning algorithms' strong nonlinear mapping ability is promising for building the relationship between IW surface signatures extracted from satellite images and IW amplitudes. Some machine learning methods have been applied to retrieve IW amplitude from optical satellite images by Pan et al. (2018) and lab data by Wang et al. (2021). Their models were trained using numerical or lab results, which are not the same as in-situ data. The accuracy of the provided true value was the upper limit of a machine learning model, so their results were limited by the truth they provided to the model and were mainly validated in shallow oceans with IW amplitudes less than 30 m.

The matched dataset between the in-situ data and satellite images was small, while the IW lab experiment provided a larger dataset. To fully utilize the two datasets, this study proposes a transfer learning model to retrieve the amplitudes of IWs from satellite images. First, we trained the model using the laboratory data collected in a water tank (Wang et al., 2021). We then applied the transfer learning technique to fine-tune the pre-trained model using limited in-situ data and synchronous satellite images. The transfer learning technique is an effective method in the machine learning field to solve the problem of small training datasets (Pan and Yang, 2009). Finally, to improve the model's performance further, we introduced a bias correction method in the model establishment that allows considering density information in real oceans. Because the lab experiment has unrealistic density differences to make the experiment easier to observe by the camera. The bias correction method can correct the pre-model results using density information in the actual oceans.

The paper is organized as follows. The data description are presented in section 2. In section 3, we show the model development and results. Applications of the model are presented in section 4. Discussions are presented in section 5, then we summarized the paper in section 6.

2 Data

2.1 Experimental lab data

IW lab experiments were conducted in a tank with a two-layer fluid system. The tank is 3 m long, 0.15 m wide, and 0.3 m tall. Two cameras were placed on the side and top of the tank to capture the IW waveform and surface signature images simultaneously. A baffle was placed 0.2 m away from the left side of the tank to generate the IW using the gravity collapse method (Du et al., 2019). On the left side of the baffle, the interface level of the water is higher than the right side. The IW was generated by the evolution of propagating vortex developed from the vertical shear movements on the left side of the tank after the baffle was removed. The generated waveform was usually consistent with the KdV equation described as:

$$\eta_t+c_0\eta_x+\alpha\eta\eta_x+\gamma\eta\eta_{xxx}=0, \tag{1}$$

$$c_0=\sqrt{\frac{2g(\rho_2-\rho_1)h_1h_2}{(\rho_2+\rho_1)H}},\quad \alpha=\frac{3c_0(h_1-h_2)}{2h_1h_2},\quad \gamma=\frac{c_0h_1h_2}{6}. \tag{2}$$

Here, g is the gravity acceleration, η is the amplitude of the solitary wave, α is the nonlinear coefficient, γ is the dispersion coefficient, c_0 is the linear phase speed, x is in the spatial variable, t is the time, $h_1(h_2)$ is the depth of the upper (lower) layer with smaller (larger) density water, and H is the total water depth. Some validations have been performed between the KdV equation and the experiment-generated IW waveform. Kao et al. (1985) presented an empirical equation to estimate the generated numbers of internal solitons in the tank, which is described as:

$$N \leqslant \frac{L}{\pi}\sqrt{\frac{3}{2}\left|\frac{h_1-h_2}{h_1^2h_2^2}\right|\eta_0}+1 \tag{3}$$

Here, L is the distance between the baffle and the left side of the tank, η_0 is the difference in the interface level of either side of the baffle. IW lab experiments have been carried out widely to study IW characteristics, such as its generation, breaking, and validation of the KdV equation (Du et al., 2019; Kao et al., 1985).

In our study, only one internal soliton was generated each time. Different amplitudes of IWs were generated under different collapse heights or stratifications, so IW data generated at different conditions could be collected. More details of the IW experiments can be found in Wang et al. (2021). During the experiment, the side-looking camera captured the waveform (amplitude) of IWs, and the down-looking camera provided synchronous surface information on the water surface where bright and dark bands were observed. A photo of the IW lab experiment is shown in Fig. 1. The side-looking camera served the in-situ data role. The down-looking camera served the satellite observation role for IWs in the natural ocean, so synchronous observation was achieved. A total of 888 pairs of IW lab data were collected.

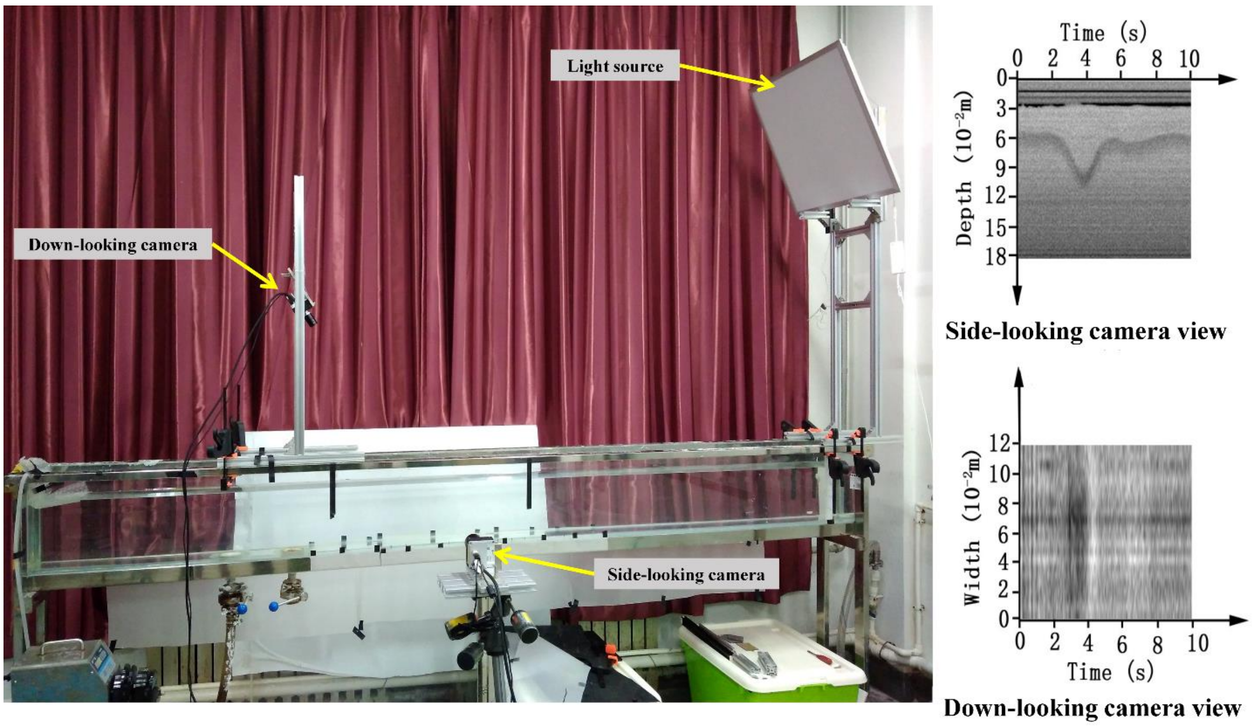

Fig. 1. Photo of the IW lab experiments and views of the two cameras.

2.2 Satellite images, in-situ data, and matched dataset

2.2.1 Satellite images

MODIS image has a swath of 2,330 km and spatial resolutions of 250 m, 500 m, and 1,000 m. Cooperation between the Terra and Aqua satellites permits two observations of the same ocean area in one day. Clear IW signatures, wide swath, and high temporal resolution make satellite observation a good choice for synchronous dataset collection. SAR images are widely used in IW observations but with a smaller swath and long revisit period. Therefore, SAR images are more difficult to match with in-situ data. In this study, MODIS images with a spatial resolution of 250 m were mainly used for collecting the synchronous observation dataset. Several synthetic aperture radar (SAR) images, such as ENVISAT ASAR images and Radarsat-2 images, collected in the South China Sea were also used to build the matched dataset (Zhang et al., 2016).

An IW will induce divergence and convergence regions on the ocean surface and hence manifest as bright or dark bands on satellite imagery. If one extracts the profiles perpendicular to the wave crest, the bright or dark bands on satellite images manifest as positive or negative peaks on the profile. The distance between the positive and negative peaks, i.e., peak-to-peak (PP) distance, can be extracted from satellite images. Previous studies have proven that the PP distance is closely related to IW amplitude (Zheng et al., 2001; Zhang et al., 2016). Therefore, the PP distance extracted from satellite images is expected to build the relationship with IW amplitude extracted from in-situ data.

2.2.2 In-situ data

In-situ data is one of the best ways to get the IW amplitude. The Andaman Sea has active IW occurrences across the ocean and multiple IW generation sites. A buoy was placed at (95.6°E, 9.6°N) to measure temperature profiles from 18 November 2012 to 28 May 2014 in the Andaman Sea (Liu et al., 2018). The underwater part of the buoy had 13 sensors continuously measuring the temperature at 1, 10, 20, 40, 60, 80, 100, 120, 140, 200, 300, 500, and 700 m depth. When an IW passed by the buoy location, the buoy observed IW-induced temperature variations.

2.2.3 Synchronous dataset – matching the in-situ data with satellite images

The total working period of the buoy in the Andaman Sea was 557 days. An IW passed by the sensor and the satellite flew over the ocean; a synchronous observation was achieved. A case of synchronous observation of IWs in the Andaman Sea using the buoy and a satellite image is shown in Fig. 2. The red dot indicates the location of the field observation. A MODIS image was collected on 11 March 2011 showing multiple IW packets propagating in different directions, with one IW packet right on the field observation spot. Corresponding field observations are shown in the lower panel of Fig. 2, where a large vertical movement of an isotherm is clearly seen. Besides the buoy placed in the Andaman Sea, in-situ observation in other oceans with matched satellite images was also collected from previous studies, such as the observations in the South China Sea (Chen et al., 2018, 2019; Huang et al., 2016; Ramp et al., 2004; Yang et al., 2009; Zhang et al., 2016), the Malin Shelf (Small et al., 1999), and the Mid-Atlantic Bight (Xue et al., 2012). Only 121 IW observation matches between in-situ data and satellite images were collected with these in-situ observations. Field observation is costly and local, and these restrictions make it difficult to collect a large synchronous dataset. Transfer learning techniques could be an excellent option to help with this problem.

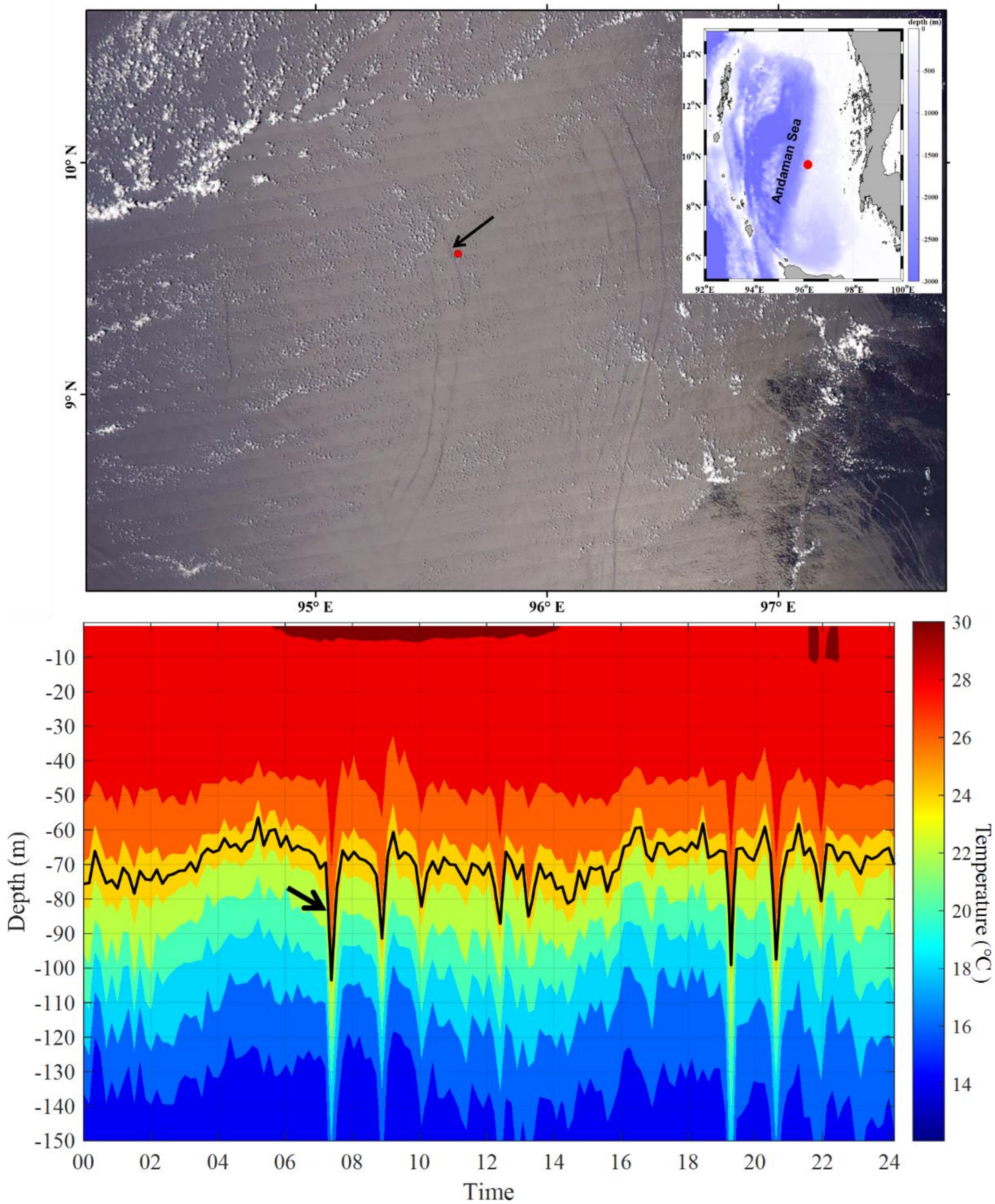

Fig. 2. Observation of IWs in the Andaman Sea using MODIS images (upper) acquired on 11 March 2011 and corresponding filed observations (lower). The red dot in the MODIS image represents the in-situ location. The solid black lines in the lower panel represent an isotherm of 25℃. The black arrow indicates the location of an IW.

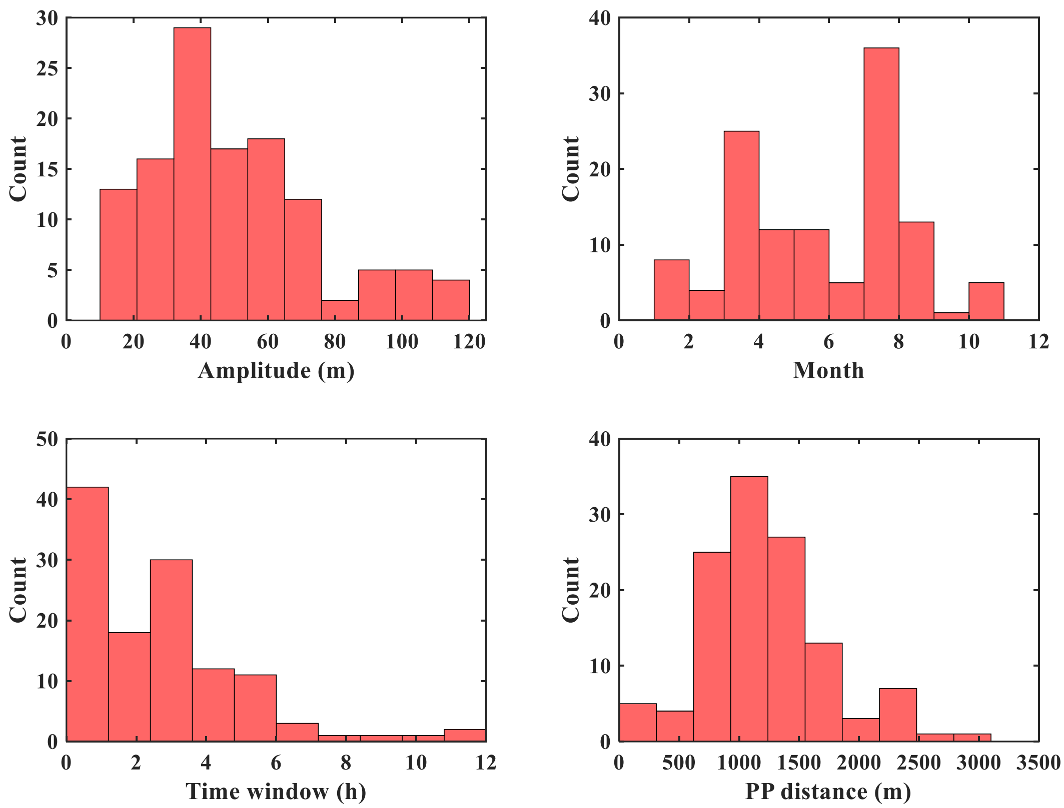

Fig. 3. Histogram of the IW amplitude, month, time window between satellite observation and in-situ observation, and the peak-to-peak distance of IWs in the collected in-situ dataset.

As shown in Fig. 3, IW amplitudes in the collected dataset range from 10 m to over 100 m, indicating both small-amplitude and large-amplitude IWs are included. The temporal distribution of collected samples shows that most samples were taken between April and August. This result is reasonable because most IWs are observed in the summer in the South China Sea and the Andaman Sea because of a stronger stratification in the summer. The in-situ data and satellite images are not perfectly synchronous, and a time window exists between them. Most of the synchronous pairs were collected with a time window of fewer than 6 hours, while some were over 10 hours. IWs are mainly periodically generated by the semi-diurnal tide in the Andaman Sea and many other oceans

(Apel et al., 1985; Zhang et al., 2021). A time window of 12 hours means an IW was generated by the successive semi-diurnal tide and might have a similar amplitude with previous ones at the exact location. This window makes it possible to match the in-situ data and satellite images in a more significant time. The PP distance of IWs is mainly between 1,000 m and 2,000 m.

3. Transfer learning model for IW amplitude retrieval

3.1 The transfer learning model

Transfer learning, which was specially proposed to solve the problem of a small dataset by utilizing a large dataset sharing similar characteristics with the target dataset, has been widely used in computer vision. For example, transfer learning has proven to be efficient for Web document classification and Wi-Fi localization when facing the problems of a few manual labels (small target dataset) and outdated data (Pan and Yang, 2009).

Here, we adopt a transfer learning technique to solve the problem of a small IW in-situ dataset. IW lab experiments were designed to study IW generation or propagation characteristics in actual oceans (Wang et al., 2021; Zhang et al., 2019). IWs data collected in the natural ocean and generated in a tank show differences, although they share similar features. This allows lab collected IW to serve as an additional data source but not as an enhanced dataset to the in-situ dataset directly. To effectively transfer the features contained in the lab data, we used transfer learning techniques. First, the lab data was used to obtain a pre-trained model; then, the pre-trained model parameters were used to initialize the final model parameters, and the in-situ data was used to fine-tune the final model. The initial parameters of the pre-trained model were randomly initialized and adjusted based on the lab data using the back-propagation algorithm, which can be described as:

$$w'_{pretrain,ki}=w_{pretrain,ki}-\alpha\frac{\partial loss_{pretrain}}{\partial w_{pretrain,ki}}, \tag{4}$$

$$loss_{pretrain}=(lab\_truth-model\_predicted_{pretrain})^2. \tag{5}$$

Here, $\alpha=0.015$ is the learning rate in our study, w is the weight of kth node in the ith layer of the neural network, the loss is used to evaluate the performance of the model prediction using truth data and its back-propagation can adjust the weights of the neural network as shown in equation (4) and (5). After the pre-trained model was established, the weights of all neural network nodes were obtained. The weights of the pre-trained model will serve as the initial weights in the fine-tuning process and the weights will be readjusted based on the in-situ data. This process can be described as:

$$W_{ft\_initial}=W_{pretrain\_final} \tag{6}$$

$$w'_{ft,ki}=w_{ft,ki}-\alpha\frac{\partial loss_{ft}}{\partial w_{ft,ki}} \tag{7}$$

$$loss_{ft}=(in\text{-}situ\_truth-model\_predicted_{ft})^2 \tag{8}$$

Here, W is the weights of all nodes in the neural network, and the subscript ‘ft’ means the fine-tuning process. The fine-tuning process made the model-learned features shift from the lab data to the in-situ data. The transfer learning technique made it possible to build a relationship between in-situ IW amplitude and satellite IW signatures (PP distance) with limited synergy with in-situ observations.

3.2 Two modifications - short connection and bias correction

We made two specially tailored modifications to the transfer learning model based on transfer learning's verified effectiveness in various fields. The first modification is the short connection between layers to avoid information loss in input parameters and promote the fitting process with a small dataset. The in-situ data used to train the model was limited. To avoid information loss during the model training process, we used the framework of a fully connected neural network incorporated with a shortcut connection to build the inversion model part. The 'shortcut connection' method was inspired by the residual module of the deep residual network (He et al., 2016). This idea has also been recently applied to image classification tasks, showing the surprisingly excellent performance (Touvron et al., 2021). The shortcut connections (blue arrows in Fig. 4) between different layers can merge features extracted in different layers, thus reducing the input information loss and ensuring better model performance. The shortcut connections can be described as:

$$v_{ki}=Relu(w_{ki}x_{ki}+b_{ki}+x_{ki-n}). \tag{9}$$

Here, v_{ki} is the output, w_{ki} is the weight, x_{ki} is the input value, and b_{ki} is the bias value of the kth node in the ith layer, x_{ki-n} is the input value of the kth node in the (i-n)th layer, n is the distance of the short connections, which indicates how many nodes are skipped to merge the inputs with the kth node, and Relu is the activation function. The nonlinear effect of the activation function will cause information loss. By merging inputs from nodes in different layers, the information loss between these layers can be reduced. The shortcut connections also benefit the model fitting process, which can help the model converge more efficiently when the dataset is small.

The second modification is to incorporate a bias correction model with the transfer learning technique to improve the model performance by introducing density information of the natural ocean. The inversion model that predicted IW amplitude was bias-corrected using two additional input parameters: the density of the upper and lower layer in actual oceans. Compared with real ocean situations, the lab experiment had unrealistic density information to make IWs easier to generate and observe by the camera. IW amplitude is affected by the ocean stratification information. The depth of the upper layer and density difference are used in the inversion model, the density information of the upper and lower layer can serve as additional information for the IW amplitude retrieval. Thus, the density information in the real ocean was used to bias correct model results. The density of the upper and lower layer and the unbias-corrected IW amplitude were inputted into the bias correction model. The relationship between the real IW amplitude and the density information can be built during the training process, so the density information can help increase the IW amplitude inversion accuracy.

Based on these two specially designed modifications, this study proposed a two-stage model, including a transfer learning inversion model and a bias correction model, to retrieve IW amplitude from satellite images. The model's loss function is the mean square error which is an appropriate indicator to evaluate the model performance in regression tasks. The detailed model structure is shown in Fig. 4.

3.3 Model inputs and outputs

IW amplitudes are relevant to ocean environment factors, such as the stratification, topography, and IW characteristics. The inputs of the first-stage model include the water depth, depth of the upper layer, relative density difference, and the PP distance extracted from satellite images (Zheng et al., 2001). The relative density difference is defined as the density difference of the upper and lower layer divided by the average density under a two-layer ocean assumption. The introduction of relative density difference aims to reduce differences between the lab and real oceans by several orders of magnitude. The PP distance is closely related to the IW amplitude, which can be extracted from satellite images and has been used to estimate IW amplitude in previous works (Zheng et al., 2001). The density and stratification information can be calculated from the publicly available monthly-mean World Ocean Atlas (WOA) 2018 dataset based on the satellite image's time, and location of an IW detected. The WOA 2018 dataset has a grid resolution of $0.25°$ and follows a standard depth level in the vertical direction. The water depth was extracted from the ETOPO1 dataset based on the IW locations. The output of the transfer learning model is the bias-corrected amplitude of IW.

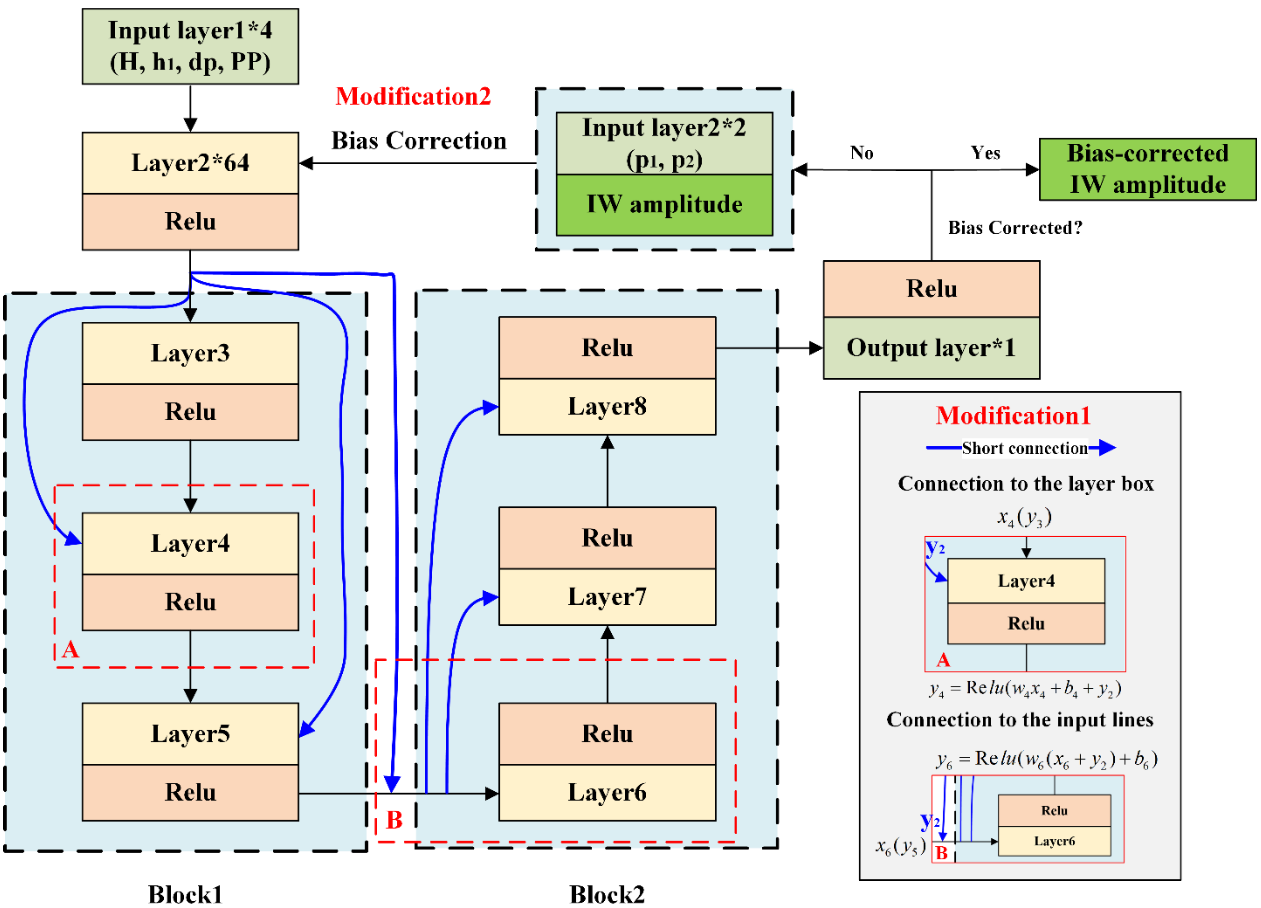

Fig. 4. Flowchart of the proposed transfer learning model to retrieve amplitude of IWs. The blue arrows indicate the shortcut connections between different layers. The width of the Block 1 and Block 2 modules is 64 (32) neurons for the inverse (bias correction) model. Two specially tailored modifications, the short connection, and the bias correction are highlighted. The IW lab and in-situ data were inputted into Input Layer 1, and the density information was inputted into Input Layer 2. In the input layers, H is the water depth, h_1 is the depth of the upper layer, dp is the density difference of upper and lower layer, PP is the IW PP distances extracted from the satellite images, ρ_1 (ρ_2) is the density of the upper (lower) layer. In the insert figure, x indicates the layer input, y

indicates the layer output, w indicates the weight of the layer, and b indicates the bias of the layer. Two different connection types are indicated with two red boxes.

3.4 Model results

The developed transfer learning IW amplitude retrieval (TLIAR) model results are shown in Fig. 5. Generally, the TLIAR model shows good agreement with the in-situ IW amplitudes in both the training and test dataset, with root mean square error (RMSE) values of 11.59 m and 9.59 m, mean relative error (MRE) values of 16% and 18%, and correlation coefficients of 0.90 and 0.89, respectively. The RMSE and MRE are defined as:

$$\mathrm{RMSE}=\sqrt{\frac{1}{\mathrm{N}}\sum_{\mathrm{i}=1}^{\mathrm{N}}(\text{True amplitude-Model predicted amplitude})^2} \tag{10}$$

$$\mathrm{MRE}=\sum\frac{\text{Model predicted amplitude - True amplitude}}{\text{True amplitude}}/\mathrm{N}\times 100 \tag{11}$$

Here, N represents the number of samples included in the calculation. The bias correction helps establish the model; the model performance improved after the bias correction was implemented. The RMSE on the test dataset decreased from 12.09 m to 9.59 m, the MRE decreased from 21% to 18%, and the correlation coefficients improved from 0.81 to 0.89. The results of the training dataset and the test dataset are very close, indicating the model is not over-fitted.

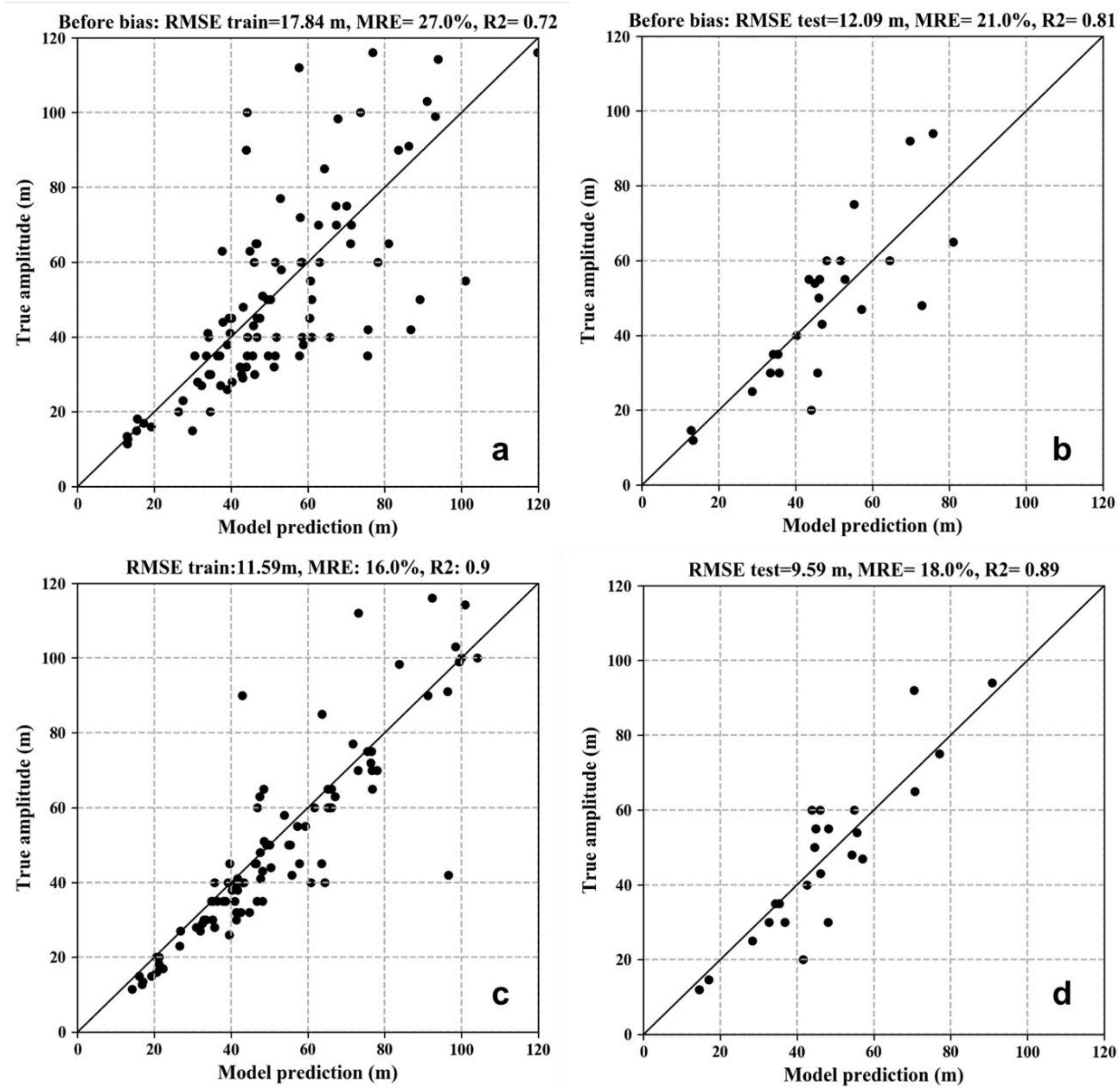

Fig. 5. TLIAR Model performance on the training (a, c) and test (b, d) dataset before (a, b) and after (c, d) bias correction. The solid black line indicates the 1-to-1 line.

Fig. 6 shows the distributions of the absolute error and the MRE with the actual IW amplitudes. A fitted line is represented with the blue line, and the red shaded area indicates the 95% confidence intervals. One can find that the absolute error increases with the increase in IW amplitude; for an IW with an amplitude of 100 m, the absolute error can be expected to be around 10 m. The fitted line for the relative error rate shows that it decreases with increased IW amplitudes; this promises that the TLIAR model still has a good performance for large-amplitude IWs. Fig. 7 shows the statistical results for IW amplitudes in different ranges, and one can find that with the increase in the IW amplitude, MRE decreases. A larger MRE for an IW amplitude of 20 m may be attributed to the smaller IWs having fewer modulations on the ocean surface and hence less prominent features on satellite images. Errors may be introduced to the PP distance of IWs. Smaller IWs may also be affected by the strong background information. For large-amplitude IWs, the IW signal is more obvious in satellite observations and ocean environments, which promise a lower MRE.

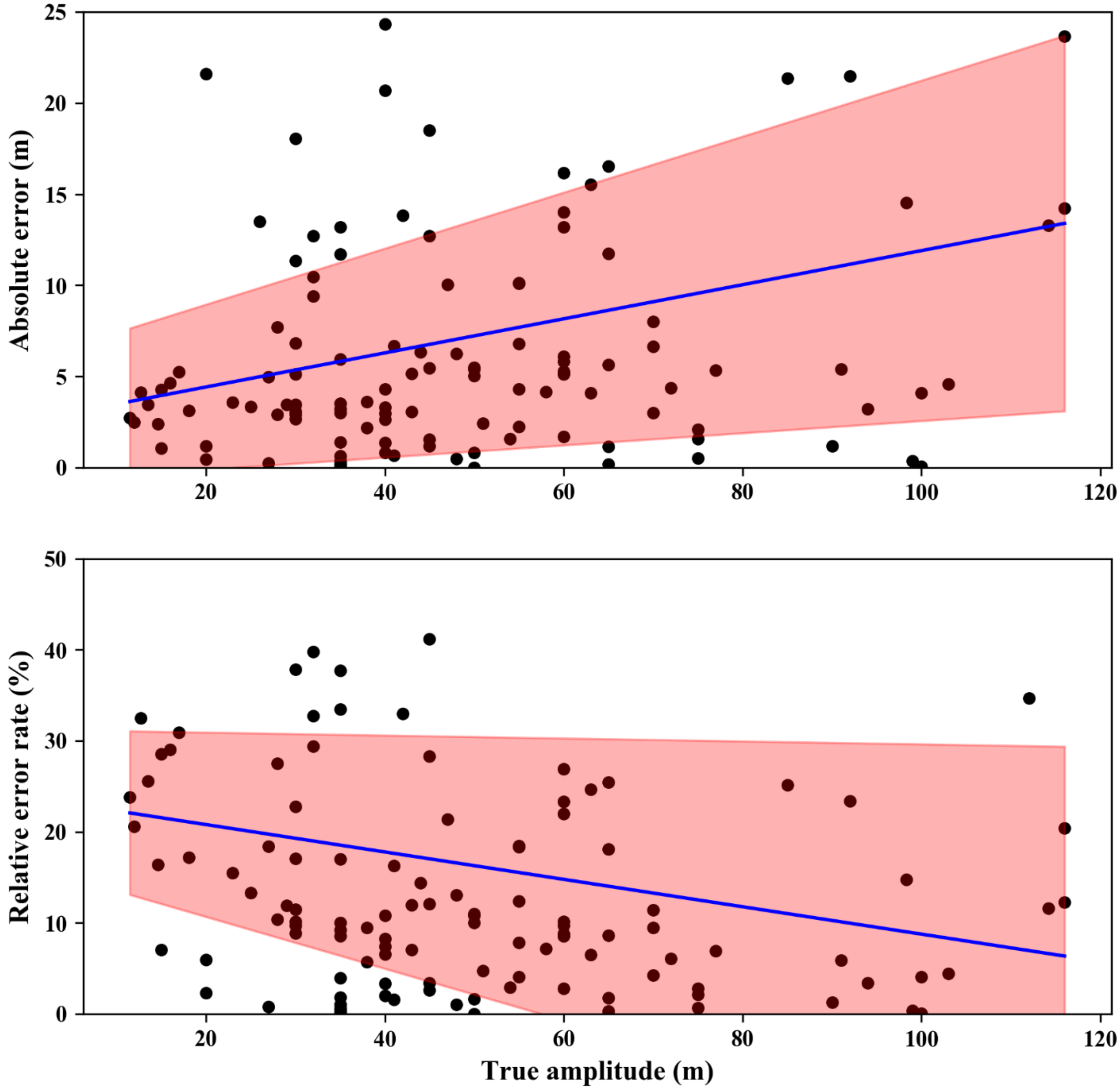

Fig. 6. Absolute error and the relative error rate of the TLIAR model. The solid blue line indicates the fitted line for the distribution, and the red shaded area indicates the 95% confidence interval.

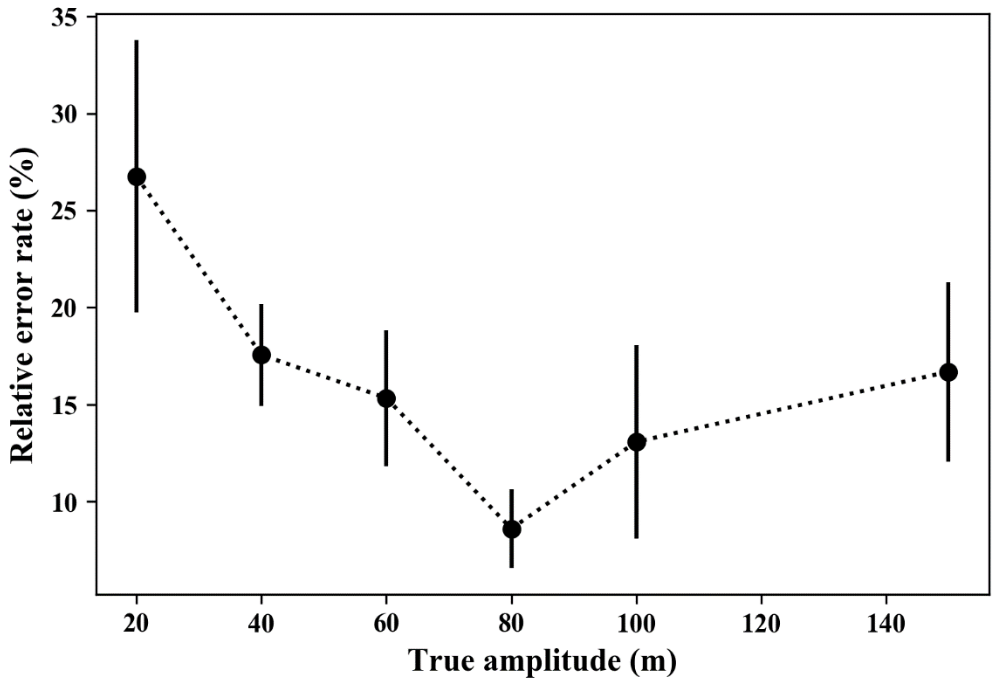

Fig. 7. The relative error rate of the TLIAR model for different IW amplitude ranges.

4. Application of the TLIAR model for IW amplitude retrieval in the Andaman Sea

The TLIAR model can retrieve IW amplitudes based on two-dimensional information extracted from satellite observations and corresponding publicly available datasets, so the three-dimensional structure of IWs was rebuilt. As shown in Fig. 8, multiple IW packets propagating eastward are observed clearly in the Andaman Sea. Three leading IWs were selected to retrieve the amplitudes using the TLIAR model. The PP distances for IW-A, IW-B, IW-C are 1,391.5 m, 731.5 m, and 517.2 m, respectively. The A, B, and C locations are shown in Fig. 8 b, and the water depth is 3,277.7 m, 1,225.5 m, and 1,592.0 m, respectively. The distance between successive IW packets is 99.02 km and 90.85 km. The amplitudes retrieved using the proposed TLIAR model are 45.8 m, 36.0 m, and 38.9 m, respectively. The three-dimensional structure of IW-A, IW-B, and IW-C are presented in Fig. 8 b. When propagating from A to B, the IW experiences a dispersion process due to the deep water, and the amplitude becomes smaller in location B than location A. When propagating from B to C, the water depth decrease gradually. The IW experiences a nonlinear process due to the nonlinear enhancing effect, so the waveform becomes steeper, and the amplitude becomes larger.

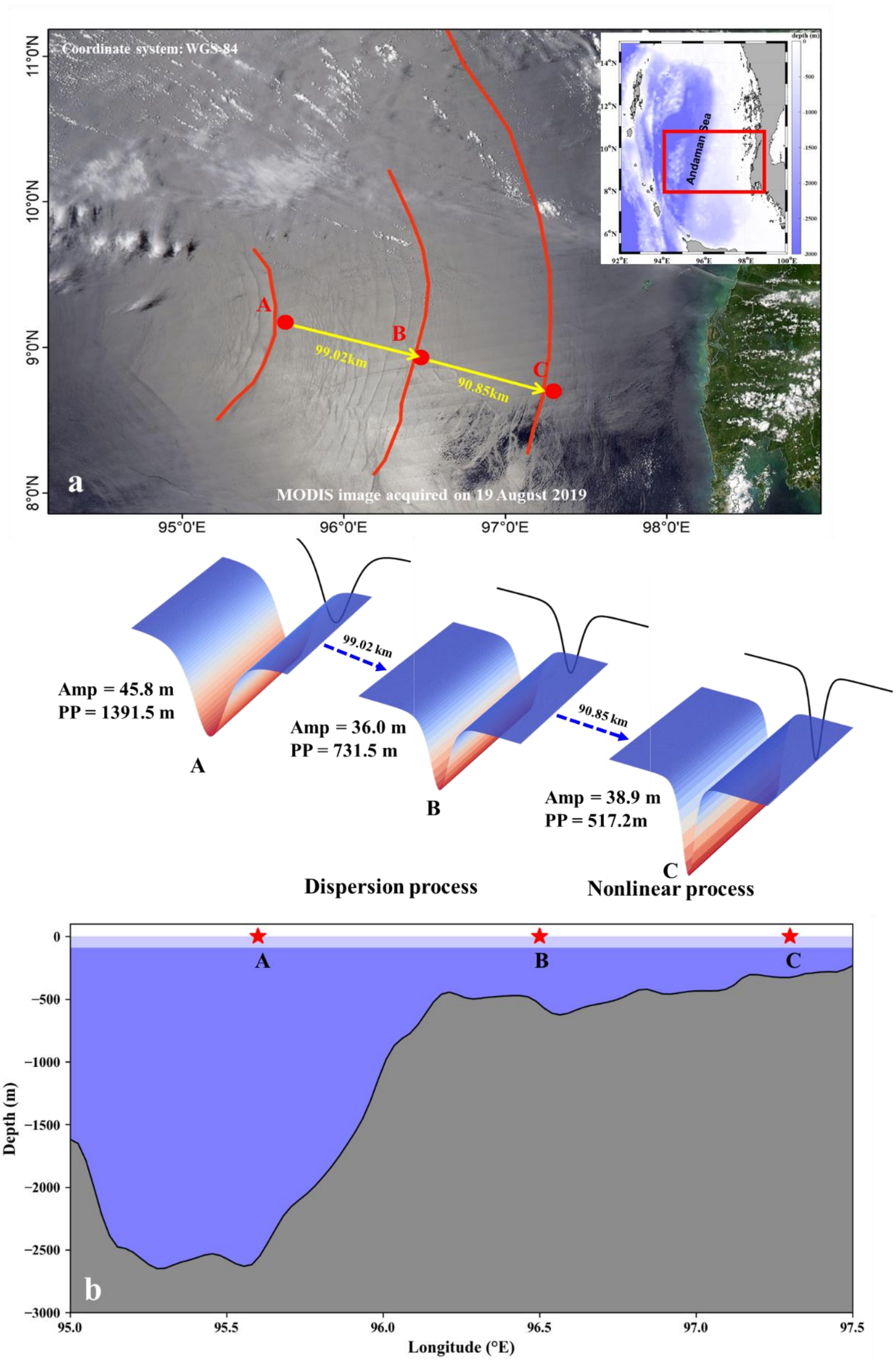

Coordinate system: WGS-84
a
MODIS image acquired on 19 August 2019
A
B
C
99.02km
90.85km
Andaman Sea
depth (m)
11°0'N
10°0'N
9°0'N
8°0'N
95°0'E
96°0'E
97°0'E
98°0'E
Amp = 45.8 m
PP = 1391.5 m
A
99.02 km
Amp = 36.0 m
PP = 731.5 m
B
90.85 km
Amp = 38.9 m
PP = 517.2m
C
Dispersion process
Nonlinear process
A
B
C
b
Depth (m)
Longitude (°E)
0
−500
−1000
−1500
−2000
−2500
−3000
95.0
95.5
96.0
96.5
97.0
97.5

Fig. 8. (a) Three IW packets observed by MODIS image taken on 19 August 2019; (b) three-dimensional structure of IWs can be obtained with model predicted amplitudes and satellite-observed PP distances with the KdV-type solutions. The underwater topography is also presented.

The proposed TLIAR model can be used to study IW amplitudes in different areas. We collected 1,097 samples from 156 satellite images in the Andaman Sea to retrieve IW amplitudes from satellite observations; a detailed description can be found in (Zhang et al., 2021). The spatial distribution of IW amplitudes and histogram of IW amplitudes are presented in Fig. 9. We can find that IW amplitudes in the Andaman Sea are mainly located at 40 m. When the IWs propagate into shallow areas with water depth less than 1,000 m, IW amplitudes increase due to the strong nonlinear effect. The nonlinear steepening of the waveform can also be found in Fig. 8. Large-amplitude IWs are mainly found at a water depth between 200 m and 1,000 m. Osborne and Burch (1980) conducted field observations in the Andaman Sea at $(6.9°\mathrm{N}, 97.0°\mathrm{W})$. They observed an IW with an amplitude of 60 m. The TLIAR model predicts IW amplitudes of about 50 m in the same location. As described in section 2, a buoy was placed at $(95.6°\mathrm{E}, 9.6°\mathrm{N})$ and field observation shows that IW amplitudes ranged from 20 m to 55 m, which is also consistent with model-predicted results (20 m to 40 m). These match results demonstrate that the proposed TLIAR model can be used to study the amplitude evolution and distribution of IWs.

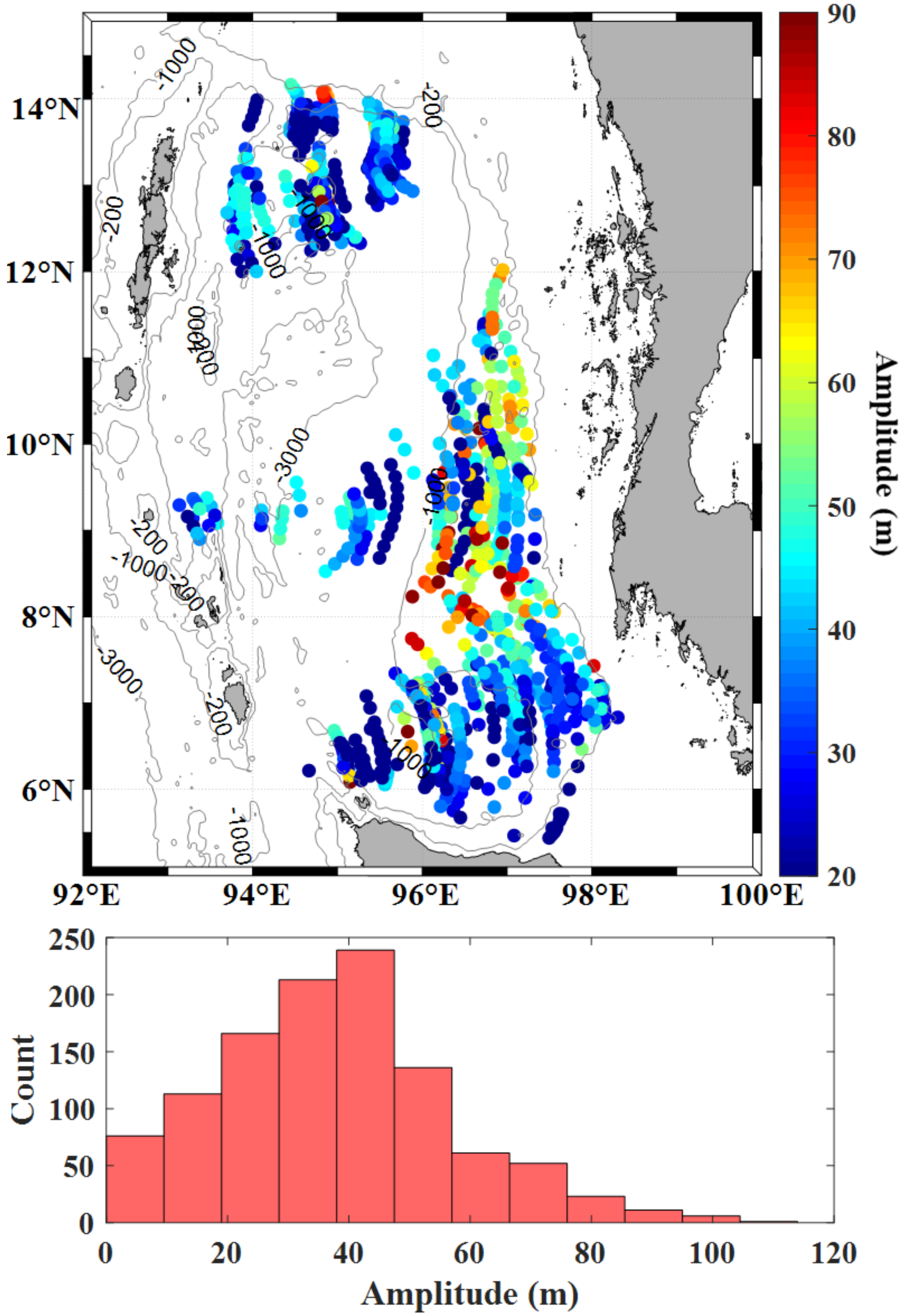

Fig. 9. Amplitude distributions (upper panel) of IWs estimated from satellite images using the TLIAR model in the Andaman Sea and corresponding histograms (lower panel).

5. Discussion

5.1 TLIAR model performance against typical machine learning models

To demonstrate the performance of our TLIAR model, we carried out more experiments comparing TLIAR with other traditional machine learning approaches. These approaches are Back-propagation neural network (BPNN), support vector machine (SVM), Random Forest (RF), and XGBoost. We firstly compare them trained by only in-situ data and then compare them trained by both lab and in-situ data. Finally, they were tested using only the in-situ data. The parameter setting and model results for different algorithms are shown in Table 1. The results show that, when only using the in-situ data to train the model, the XGboost algorithm had the best performance on the independent test dataset with the smallest RMSE of 18.70 m. On the other hand, as shown in section 3, the TLIAR model has an RMSE of 9.59 m, and this result demonstrates that the introduction of the lab data is valuable and necessary.

Table 1. Performance of different algorithms trained by only the in-situ data

Models	Parameter setting	RMSE_train(m)	RMSE_test(m)
BPNN	Four-hidden-layer structure: 32, 16, and 8 activation function: relu	24.24	24.53
SVM	C=40, Kernel=rbf, gamma=0.6	20.50	21.64
RF	n_estimators=100, max_depth=30	7.31	19.59
XGBoost	max_depth=5, min_child_weight=3, learning_ rate=0.15, n_estimators=120, gamma=0.18	12.36	18.70

Seven different fusion data/model strategies were applied to compare their performance to combine the lab collected data and in-situ data. The details of combining the lab and in-situ data are listed in Table 2.

Table 2. Descriptions of different fusion strategies to combine the lab and in-situ data.

Strategy	Index	Description
One model	F1	Lab data and observational data were trained together directly.
	F2	Lab data and observational data were normalized separately and then put together for the model training.
	F3	The amplitudes and PP distances were normalized using the water depth for both the lab data and observational data, then put together for the model training.
	F4	A scaling factor was calculated based on the median or average IW amplitudes in the lab data and observational data. The lab data were rescaled before putting the data together.
	F5	The IW amplitudes were normalized using the water depth, and the PP distances were normalized using the upper water depth; then the data were put together for the model training.
Stacking model	F6	A lab model was trained using the lab data; the lab model predicted IW amplitude served as one of the input parameters of the observational model; the observational model produced the final predicted IW amplitudes.

	F7	A lab model and an observational model were trained separately using the lab data and observational data. The predicted IW amplitudes served as input parameters for a third emerged model, which produced the final predicted IW amplitudes.

The fusion strategies include five one-model strategies and two stacking-model strategies. The one-model strategy combined the data and was used for training in a single model. The stacking-model strategy built multiple models using different data sources as a stacking model. As shown in Table 1, the XGBoost has the best performance among those models; we tested different fusion strategies based on the XGboost model. The performance of different fusion strategies is shown in Table 3. The performance of different strategies had similar RMSE values on the test dataset, all over 20.0 m. Compared with the models trained only using in-situ data, the fusion strategies do not show apparent improvements when more lab data were included in the training dataset. However, the proposed transfer learning TLIAR model showed much better performance than models F1-F7, with RMSE of 11.59 m and 9.59 m on the training and test dataset. The comparison demonstrates that the transfer learning technique is an efficient way to overcome small dataset problems for IW studies.

Table 3. Model performance for different fusion strategies.

Fusion Strategy		**RMSE_train (m)**	**RMSE_test (m)**
One model	F1	4.57	20.84
	F2	3.77	23.48

	F3	3.82	24.63
	F4	12.39	20.09
	F5	16.38	22.66
Stacking model	F6	12.79	20.99
	F7	9.62	21.68

5.2 Influence of input parameter noise

The TLIAR model has many input parameters, and errors may be introduced. The water depth was extracted from ETOPO1, and stratification data was extracted from the WOA 2018 dataset. Errors should not be very substantial for input parameters extracted from these publicly published datasets. The PP distance was measured from satellite images and may have been affected by complex imaging conditions and backgrounds. Therefore, errors in the PP distance extracted from satellite images were more easily introduced. The MODIS images used in this study had a spatial resolution of 250 m. Here we consider an error of two pixels (±500 m) on the MODIS image to investigate its influence on the model performance, and the results are shown in Fig. 10. The model performance degraded from 10 m to less than 20 (25) m with an error of 250 m (500 m). As shown in Fig. 3, the PP distance mainly ranged from 1,000 m to 2,000 m. An error of 500 m indicates a 32 - 50% error rate on the PP distance measurements. The correlation coefficient and MRE degraded to over 0.7 (0.4) and 30% (40%), respectively, with an error of 250 m (500 m). With a one-pixel-error on the PP distance, the model generally produces a reliable result, while with two-pixel-error, the model shows relatively large deviations. Although the TLIAR model shows good tolerance on the PP distance error, we can still further reduce the error of PP distance measurements.

SAR images have a higher spatial resolution (tens of meters), which reduces the PP distance error. The PP distance error was also reduced when we extracted multiple profiles and obtained the average measurement. Therefore, while the TLIAR model shows strong robustness on PP distance errors, we can still take several measurements to further reduce the measurement error, which promised good performance from the TLIAR model.

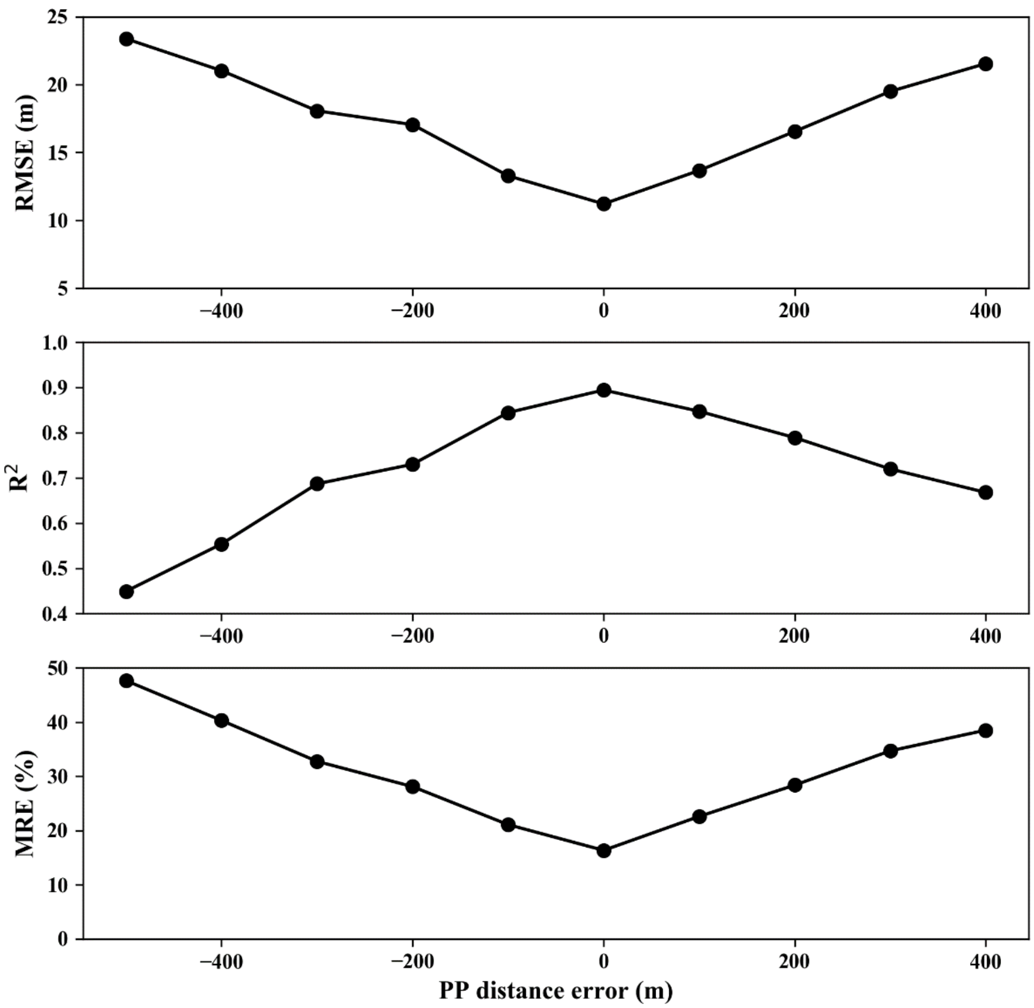

Fig. 10. The TLIAR model performance for PP distance input errors.

5.3 Comparison with the KdV equation-based method

The KdV equation has been widely applied to retrieve internal solitary wave amplitude (Zhao et al., 2004; Zheng et al., 2001). The KdV equation for the propagation of the internal solitary wave is described in equation (1). Equation (1) has a soliton solution described as:

$$\eta(x,t)=\eta_0 \mathrm{sech}^2\left[\frac{x-vt}{L}\right]$$

$$L=\sqrt{\frac{12\gamma}{\alpha\eta_0}} \tag{12}$$

where η_0 is the maximum amplitude, and L is the characteristic half-width. Zheng et al. (2001) proposed the relationship between the internal solitary wave half-width and the PP distance extracted from satellite images. As shown in Fig.2, an IW was observed on the MODIS image near the buoy. The IW has a PP distance of 1,241.93 m with an in-situ amplitude of 35 m. The TLIAR model-predicted amplitude is 38.45 m, while the KdV-predict amplitude is 25.01 m. Another case is shown in Fig. 11, a MODIS image was acquired at 06:59 on 27 March 2013, and the PP distance is 1,916.13 m. The buoy captured the IW about 1 hour later with an amplitude of 43 m. The TLIAR model-predicted IW amplitude is 38.45 m, while the KdV-predicted amplitude is 10.50 m. The KdV prediction show much more significant deviations than the proposed TLIAR model. As shown in Fig.3, the PP distance of IWs mainly ranges from 1,000 m to 2,000 m, and the KdV equation generally produces minimal amplitude inversion results.

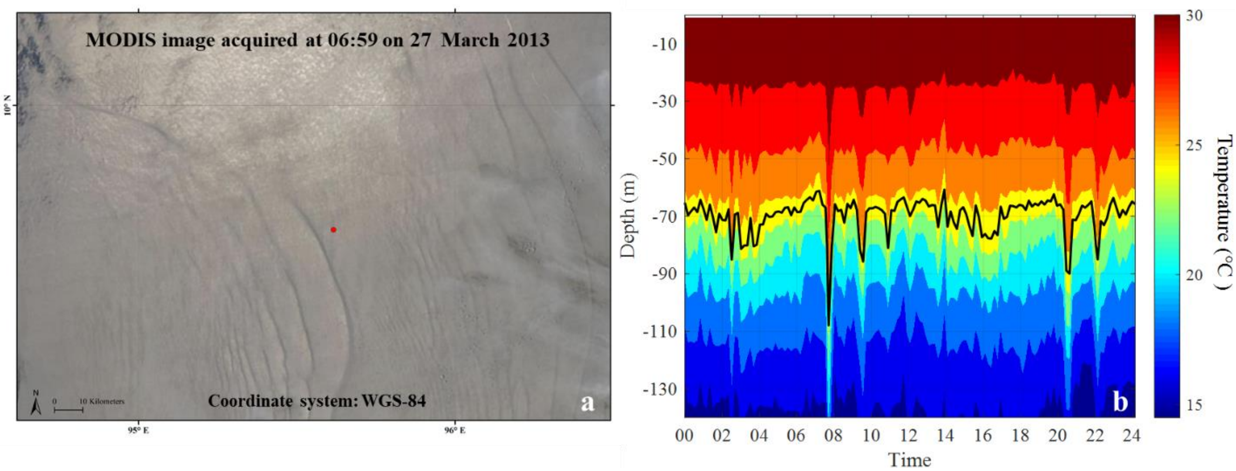

Fig. 11. Observation of IWs in the Andaman Sea using MODIS images (a) acquired at 06:59 on 27 March 2013 and the corresponding in-situ data (b). The red dot indicates the buoy location.

The KdV equation is mainly suitable for small-amplitude internal solitary waves in shallow oceans. Now we analyze which regimes the collected dataset fell in. Considering the average results, the horizontal length scale (L) was 2,000 m, the depth of the upper layer (h) was 60 m, the total water depth (H) was 1,258 m, and the amplitude (A) was 50 m. We calculated $L/H \sim O(1)$, $h/H \ll 1$, $AL^2/H^3 \ll 1$, $AL/h^2 \gg 1$. This result does not fall in the regime of the shallow-water theory, deep-water theory, or the finite-depth theory demonstrating that IWs in the ocean are more complicated than can be modeled using the KdV or extended equations.

5.4 TLIAR model applicability for extra-large-amplitude IWs

As shown in Fig. 3, IW amplitude in the collected matched dataset ranged from tens of meters to over 100 meters. The largest IW amplitude in the matched in-situ dataset was 116 m. IW amplitudes in the South China Sea and other oceans reached over 200 m. The performance of the TLIAR model for extra-large-amplitude IWs was not validated in this study because we did not find such data to train or test the model. However, according to the results shown in Fig. 6, the relative error rate decreased with increased IW amplitudes. If more data is collected in the future, the model could be tested or even re-trained based on the same approach.

5.5 Model application to other ocean areas

The TLIAR model was developed mainly based on the matched dataset in the Andaman Sea, while some data in other ocean areas were also included. The water depth variations for the developed model ranges from 75 m to 2789 m, the mixed layer depth ranges from 13 m to 95 m, the density of the upper layer ranges from $1021\ \mathrm{kg/m^3}$ to $1023\ \mathrm{kg/m^3}$, and the density of the lower layer ranges from $1024\ \mathrm{kg/m^3}$ to $1027\ \mathrm{kg/m^3}$. The model was trained and tested under a wide range of ocean conditions. The model should not apply to only one region. We show a few examples below.

A MODIS image acquired on 28 August 2014 showing clear IW signatures in the South China Sea was reported in the work of Xu et al. (2020), as shown in Fig. 12. The water depth at the observation location is 1180 m. The depth of the upper layer extracted from the WOA2018 is 65 m, close to in-situ data. The PP distance of the nearest leading IW in Fig. 12 is 647.83 m. The TLIAR model estimated IW amplitude is 99.6 m, while the in-situ IW amplitude is close to 100 m (Fig. 6i in Xu et al., 2020), which shows good agreements between the model result and in-situ data. This result indicates that the developed TLIAR model works well in the South China Sea.

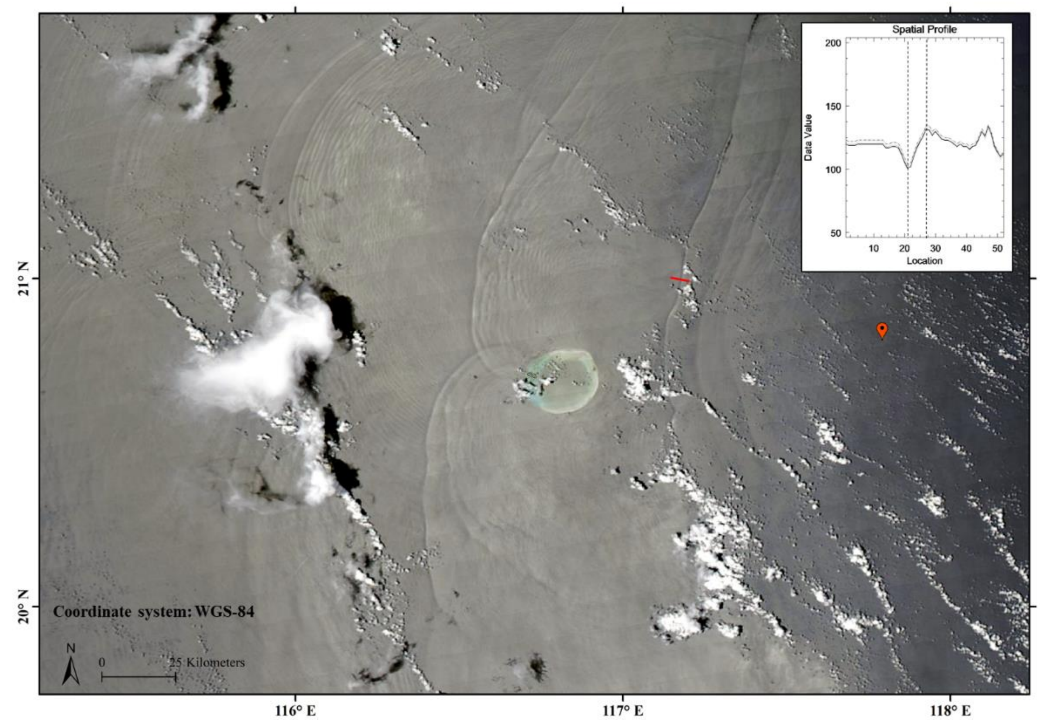

Fig. 12. MODIS image acquired on 28 August 2014 showing clear IW signatures in the South China Sea. The red symbol indicates the in-situ observation location reported in Xu et al. (2020). The insert map shows the extracted profiles indicated by the solid red line.

Data in the South China Sea is included during the model establishment, no sample is located in the Sulu Sea in the matched in-situ dataset. To test the model applicability in the Sulu Sea, we used MODIS images reported in Zhang et al. (2020) to inverse IW amplitudes, and the results are shown in Fig. 13. Historical in-situ data were used to validate the model results because no in-situ data is found in the Sulu Sea. The black box in Fig. 13 represents the in-situ observation station, SS3, reported in Apel et al. (1985). IWs in the SS3 station observed 18 solitons with amplitudes ranging from 20 m to 80 m (Fig. 20 in Apel et al., 1985). The histogram of TLIAR model results of IWs in this area is shown in the right panel of Fig. 13, where IW amplitudes show good agreements with historical in-situ observations in the Sulu Sea. Although we do not test the model applicability further, existing results show the model works reasonably well.

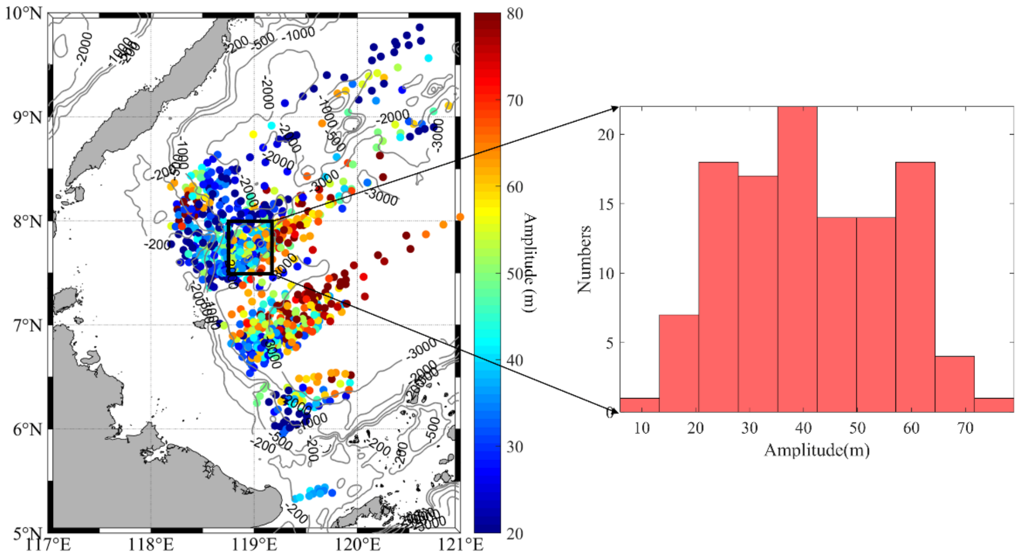

Fig. 13. Amplitude distributions (left) of IWs estimated using the TLIAR model in the Sulu Sea. The black box indicates the SS3 station in Apel et al. (1985). The right panel shows the corresponding IW amplitude histograms in the black box.

6 Conclusions

Amplitude is an important parameter for IW studies. In this study, a transfer learning model was proposed to invert IW amplitudes from satellite images. To develop the model, we built two datasets, including 888 pairs of IW lab data and 121 pairs of satellite/in-situ matched datasets. The TLIAR model is a two-stage model including an inversion model and a bias correction model. We introduced the transfer learning technique and short connection in the inversion model. The transfer learning helps to utilize two datasets fully, and the short connection helps to reduce the information loss and makes the model convergence easier. The bias correction used the density information in the natural ocean to correct the results of the inversion model. The model has an RMSE of 9.59 m, an MRE of 18%, and a correlation coefficient of 0.89 on an independent test dataset, which shows good consistency between the model predictions and field observations. Analysis shows that for an IW with a large amplitude of 100 m, the absolute error is expected to be around 10 m. Relative error rate analysis shows that the TLIAR model still has good performance for large-amplitude IWs. The model was applied to IW amplitude retrievals in the Andaman Sea. The spatial distributions and variations of IW amplitude were revealed: IW amplitudes in the Andaman Sea are mainly located at 40 m, and large-amplitude IWs are mainly found at a water depth between 200 m and 1,000 m.

Five other machine learning algorithms also join the experiments. Each algorithm built one model trained with only in-situ data, and seven fusion models trained with lab and in-situ data were tested. The XGBoost model has the best performance for models trained with only in-situ data, with an RMSE of 18.70 m. Considering an RMSE of 9.59 m for the TLIAR model, the introduction of the lab data was necessary. Seven fusion models did not improve, while the TLIAR model showed far better performance. These results demonstrate that the lab data serves as an excellent additional data source, and the transfer learning technique is efficient for this study.

The error distribution with the IW amplitudes was also presented, and the results indicate that the model can still have a small error for IW amplitude over 100 m. However, the error rate was reduced for large-amplitude IWs. Noise sensitivity analysis shows that while the noise is most easily introduced to the PP distance, the model shows large tolerance for the PP distance error, with a one-pixel error and RMSE still less than 20 m. Compared with the KdV equation, the TLIAR model shows a much better result. Model applicability in the Sulu Sea was also discussed, the model results show good agreements with historical in-situ results.

Author responsibility

Xudong Zhang and Xiaofeng Li designed the study. Xudong Zhang, Haoyu Wang, and Shuo Wang contributed to the model realization. Weidong Yu, Yanliang Liu, and Jing Wang contribute to the in-situ and lab data processing. All authors contributed to the writing, discussion, and revision of the paper.

Acknowledgments

This work was supported by the CAS (Chinese Academy of Sciences) Program [grant number Y9KY04101L], the Strategic Priority Research Program of the Chinese Academy of Sciences [grant number XDB42000000]; Key Project of Center for Ocean Mega-Science [grant number COMS2019R02]; the National Natural Science Foundation for Young Scientists of China [grant number 41906157]; National Natural Science Foundation of China [grant numbers U2006211, 42090044, 41776183]; Major scientific and technological innovation projects in Shandong Province [grant number 2019JZZY010102]; and supported by UK Royal Society International Exchange Project [grant number IES\R1\211036].

The buoy data were provided by the regional international cooperation project Monsoon Onset Monitoring and its Social and Ecosystem Impact (MOMSEI). MODIS images of Terra and Aqua were downloaded from NASA's LAADS Web (https://ladsweb.modaps.eosdis.nasa.gov/search/). The water depth data were downloaded from the ETOPO1 Global Relief Model

(https://maps.ngdc.noaa.gov/viewers/wcs-client/). The stratification data was obtained from the World Ocean Atlas 2018 (https://www.nodc.noaa.gov/OC5/woa18/).

References

Alford, M.H., Lien, R.C., Simmons, H., Klymak, J., Ramp, S., Yang, Y.J., Tang, D., Chang, M.H., 2010. Speed and evolution of nonlinear internal waves transiting the South China Sea. J. Phys. Oceanogr. 40, 1338-1355.

Alpers, W., 1985. Theory of radar imaging of internal waves. Nature 314, 245-247.

Apel, J.R., Holbrook, J.R., Liu, A.K., Tsai, J.J., 1985. The Sulu Sea internal soliton experiment. J. Phys. Oceanogr. 15, 1625-1651.

Bai, X., Li, X., Lamb, K.G., Hu, J., 2017. Internal solitary wave reflection near Dongsha Atoll, the South China Sea. J. Geophys. Res. Oceans 122, 7978-7991.

Chen, L., Zheng, Q., Xiong, X., Yuan, Y., Xie, H., 2018. A new type of internal solitary waves with a re-appearance period of 23 h observed in the South China Sea. Acta Oceanol. Sin. 37, 116-118.

Chen, L., Zheng, Q., Xiong, X., Yuan, Y., Xie, H., Guo, Y., Yu, L., Yun, S., 2019. Dynamic and statistical features of internal solitary waves on the continental slope in the northern South China Sea derived from mooring observations. J. Geophys. Res. Oceans 124, 4078-4097.

da Silva, J., Magalhaes, J., Gerkema, T., Maas, L., 2012. Internal solitary waves in the Red Sea: an unfolding mystery. Oceanography 25, 96-107.

Du H., Wei G., Wang S., Wang, X., 2019. Experimental study of elevation-and depression-type internal solitary waves generated by gravity collapse. Phys. Fluids, 31(10): 102104.

Guo, C., Vlasenko, V., Alpers, W., Stashchuk, N., Chen, X., 2012. Evidence of short internal waves trailing strong internal solitary waves in the northern South China Sea from synthetic aperture radar observations. Remote Sens. Environ. 124, 542-550.

He, K., Zhang, X., Ren, S., Sun, J., 2016. Deep residual learning for image recognition. In, Proceedings of the IEEE Conference on Computer Vision and Pattern Recognition (pp. 770-778)

Huang, X., Chen, Z., Zhao, W., Zhang, Z., Zhou, C., Yang, Q., Tian, J., 2016. An extreme internal solitary wave event observed in the northern South China Sea. Sci. Rep. 6, 30041.

Xu, J., He, Y., Chen, Z., Zhan, H., Wu, Y., Xie, J., Shang, X.,Ning, D., Fang, W., Cai, S., 2020. Observations of different effects of an anti-cyclonic eddy on internal solitary waves in the South China Sea. Prog. Oceanogr., 188, 102422.

Kao T.W., Pan F.S., Renouard D., 1985. Internal solitons on the pycnocline: generation, propagation, and shoaling and breaking over a slope. J. Fluid Mech., 159: 19-53.

Kozlov, I., Romanenkov, D., Zimin, A., Chapron, B., 2014. SAR observing large-scale nonlinear internal waves in the White Sea. Remote Sens. Environ. 147, 99-107.

Lavrova, O., Mityagina, M., 2017. Satellite survey of internal waves in the Black and Caspian Seas. Remote Sens. 9, 892.

Li, X., Jackson, C.R., Pichel, W.G., 2013. Internal solitary wave refraction at Dongsha Atoll, South China Sea. Geophys. Res. Lett. 40, 3128-3132.

Li, X., Liu, B., Zheng, G., Ren, Y., Zhang, S., Liu, Y., Gao, L., Liu, Y., Zhang, B., Wang, F., 2020. Deep-learning-based information mining from ocean remote-sensing imagery. Natl. Sci. Rev. 7, 1584-1605.

Li, X., Zhao, Z., Pichel, W.G., 2008. Internal solitary waves in the northwestern South China Sea inferred from satellite images. Geophys. Res. Lett. 35, L13605.

Lindsey, D.T., Nam, S., Miller, S.D., 2018. Tracking oceanic nonlinear internal waves in the Indonesian seas from geostationary orbit. Remote Sens. Environ. 208, 202-209.

Liu, A.K., Chang, Y.S., Hsu, M.K., Liang, N.K., 1998. Evolution of nonlinear internal waves in the East and South China Seas. J. Geophys. Res. Oceans 103, 7995-8008.

Liu, A.K., Hsu, M.K., 2004. Internal wave study in the South China Sea using Synthetic Aperture Radar (SAR). Int. J. Remote Sens. 25, 1261-1264.

Liu, A.K., Ramp, S.R., Zhao, Y.H., Tang, T.Y., 2004. A case study of internal solitary wave propagation during ASIAEX 2001. IEEE J. Ocean. Eng. 29, 1144-1156.

Liu, B., Yang, H., Zhao, Z., Li, X., 2014. Internal solitary wave propagation observed by tandem satellites. Geophys. Res. Lett. 41, 2077-2085.

Liu, Y., Li, K., Ning, C., Yang, Y., Wang, H., Liu, J., Skhokiattiwong, S., Yu, W., 2018. Observed seasonal variations of the upper ocean structure and air-sea interactions in the Andaman Sea. J. Geophys. Res. Oceans 123, 922-938.

Marghany, M., 1999. Internal wave detection and wavelength estimation. In: IEEE 1999 Int. Geosci. Remote Sen. Symp. 1999-June, 163-165.

Marghany, M., 2018. Automatic detection of internal wave using particle swarm optimization algorithm. In: IOP Conference Series: Earth and Environmental Science. 2018-June,169 (1), 012049.

Marghany, M., 2021. Nonlinear Ocean Dynamics: Synthetic Aperture Radar, first ed. Elsevier.

Magalhaes, J., da Silva, J., 2018. Internal solitary waves in the Andaman Sea: new insights from SAR imagery. Remote Sens. 10, 861.

Magalhaes, J., Pires, A., da Silva, J., Buijsman, M., Oliveira, P., 2021. Using SAR imagery to survey internal solitary wave interactions: a case study off the Western Iberian shelf. Cont. Shelf Res. 220, 104396.

Magalhaes, J.M., da Silva, J.C.B., Buijsman, M.C., 2020. Long lived second mode internal solitary waves in the Andaman Sea. Sci. Rep. 10, 10234.

Osborne, A.R., Burch, T.L., 1980. Internal solitons in the Andaman Sea. Science 208, 451-460.

Pan, S.J., Yang, Q., 2009. A survey on transfer learning. IEEE T. Knowl. Data En. 22, 1345-1359.

Pan, X., Wang, J., Zhang, X., Mei, Y., Shi, L., Zhong, G., 2018. A deep-learning model for the amplitude inversion of internal waves based on optical remote-sensing images. Int. J. Remote Sens. 39, 607-618.

Ramp, S.R., Tang, T.Y., Duda, T.F., Lynch, J.F., Liu, A.K., Chiu, C.S., Bahr, F.L., Kim, H.R., Yang, Y.J., 2004. Internal solitons in the northeastern South China Sea. Part I: Sources and deep water propagation. IEEE J. Ocean. Eng. 29, 1157-1181.

Scotti, A., Beardsley, R.C., Butman, B., Pineda, J., 2008. Shoaling of nonlinear internal waves in Massachusetts Bay. J. Geophys. Res. Oceans 113, C08031.

Serebryany, A., Khimchenko, E., Popov, O., Denisov, D., Kenigsberger, G., 2020. Internal waves study on a narrow steep shelf of the Black Sea using the spatial antenna of line temperature sensors. J. Mar. Sci. Eng. 8(11), 833.

Shroyer, E.L., Moum, J.N., Nash, J.D., 2011. Nonlinear internal waves over New Jersey's continental shelf. J. Geophys. Res. Oceans 116, C03022.

Small, J., Hallock, Z., Pavey, G., Scott, J., 1999. Observations of large amplitude internal waves at the Malin Shelf edge during SESAME 1995. Cont. Shelf Res. 19, 1389-1436.

Tensubam, C.M., Raju, N.J., Dash, M.K., Barskar, H., 2021. Estimation of internal solitary wave propagation speed in the Andaman Sea using multi–satellite images. Remote Sens. Environ. 252, 112123.

Touvron, H., Bojanowski, P., Caron, M., Cord, M., El-Nouby, A., Grave, E., Joulin, A., Synnaeve, G., Verbeek, J., Jégou, H., 2021. Resmlp: Feedforward networks for image classification with data-efficient training. arXiv preprint arXiv:2105.03404.

Wang, J., Zhang, M., Mei, Y., Lu, K., Chen, X., 2021. Study on inversion amplitude of internal solitary waves applied to shallow sea in the laboratory. IEEE Geosci. Remote. Sens. Lett. 18, 577-581.

Xue, J., Graber, H.C., Lund, B., Romeiser, R., 2012. Amplitudes estimation of large internal solitary waves in the Mid-Atlantic Bight using synthetic aperture radar and marine X-band radar images. IEEE Trans. Geosci. Remote Sensing 51, 3250-3258.

Xue, J., Graber, H.C., Romeiser, R., Lund, B., 2014. Understanding internal wave–wave interaction patterns observed in satellite images of the Mid-Atlantic Bight. IEEE Trans. Geosci. Remote Sensing 52, 3211-3219.

Xu, Q., Zheng, Q., Lin, H., Liu, Y., Song, Y.T., Yuan, Y., 2008. Dynamical analysis of mesoscale eddy-induced ocean internal waves using linear theories. Acta Oceanol. Sin. 27, 60-69.

Yang, Y.J., Fang, Y.C., Chang, M.H., Ramp, S.R., Kao, C.C., Tang, T.Y., 2009. Observations of second baroclinic mode internal solitary waves on the continental slope of the northern South China Sea. J. Geophys. Res. Oceans 114

Zhang, X., Wang, J., Sun, L., Meng, J., 2016. Study on the amplitude inversion of internal waves at Wenchang area of the South China Sea. Acta Oceanol. Sin. 35(7), 14-19.

Zhang, M., Wang, J., Chen, X., Mei, Y., Zhang, X., 2019. An experimental study on the characteristic pattern of internal solitary waves in optical remote-sensing images. Int. J. Remote Sens. 40, 7017-7032.

Zhang, X., Li, X., 2021. Combination of satellite observations and machine learning method for internal wave forecast in the Sulu and Celebes Seas. IEEE Trans. Geosci. Remote Sensing 59, 2822-2832.

Zhang, X., Li, X., Zhang, T., 2020. Characteristics and generations of internal wave in the Sulu Sea inferred from optical satellite images. J. Oceanol. Limnol. 38, 1435-1444.

Zhang, X., Li, X., Zheng, Q., 2021. A machine-learning model for forecasting internal wave propagation in the Andaman Sea. IEEE J. Sel. Top. Appl. Earth Obs. Remote Sens. 14, 3095-3106.

Zhao, Z., Klemas, V., Zheng, Q., Li, X., Yan, X., 2004. Estimating parameters of a two-layer stratified ocean from polarity conversion of internal solitary waves observed in satellite SAR images. Remote Sens. Environ. 92, 276-287.

Zhao, Z., Liu, B., Li, X., 2014. Internal solitary waves in the China seas observed using satellite remote-sensing techniques: a review and perspectives. Int. J. Remote Sens. 35, 3926-3946.

Zheng, G., Li, X., Zhang, R., Liu, B., 2020. Purely satellite data–driven deep learning forecast of complicated tropical instability waves. Sci. Adv. 6, eaba1482.

Zheng, Q., Yuan, Y., Klemas, V., Yan, X., 2001. Theoretical expression for an ocean internal soliton synthetic aperture radar image and determination of the soliton characteristic half width. J. Geophys. Res. Oceans 106, 31415-31423.

Zubkova, E. V., Kozlov, I. E., 2020. Characteristics of short-period internal waves in the Chukchi Sea based on spaceborne SAR observations. Sovrem. Probl. Distantsionnogo Zondirovaniya Zemli iz Kosm. 17(4), 221-230.

List of Figure Captions

Fig. 1. Photo of the IW lab experiments and views of the two cameras.

Fig. 2. Observation of IWs in the Andaman Sea using MODIS images (upper) acquired on 11 March 2011 and corresponding filed observations (lower). The red dot in the MODIS image represents the in-situ location. The solid black lines in the lower panel represent an isotherm of 25℃. The black arrow indicates the location of an IW.

Fig. 3. Histogram of the IW amplitude, month, time window between satellite observation and in-situ observation, and the peak-to-peak distance of IWs in the collected in-situ dataset.

Fig. 4. Flowchart of the proposed transfer learning model to retrieve amplitude of IWs. The blue arrows indicate the shortcut connections between different layers. The width of the Block 1 and Block 2 modules is 64 (32) neurons for the inverse (bias correction) model. Two specially tailored modifications, the short connection, and the bias correction are highlighted. The IW lab and in-situ data were inputted into Input Layer 1, and the density information was inputted into Input Layer 2. In the input layers, H is the water depth, h_1 is the depth of the upper layer, dp is the density difference of upper and lower layer, PP is the IW PP distances extracted from the satellite images, p_1 (p_2) is the density of the upper (lower) layer. In the insert figure, x indicates the layer input, y indicates the layer output, w indicates the weight of the layer, and b indicates the bias of the layer. Two different connection types are indicated with two red boxes.

Fig. 5. TLIAR Model performance on the training (a, c) and test (b, d) dataset before (a, b) and after (c, d) bias correction. The solid black line indicates the 1-to-1 line.

Fig. 6. Absolute error and the relative error rate of the TLIAR model. The solid blue line indicates the fitted line for the distribution, and the red shaded area indicates the 95% confidence interval.

Fig. 7. The relative error rate of the TLIAR model for different IW amplitude ranges.

Fig. 8. (a) Three IW packets observed by MODIS image taken on 19 August 2019; (b) three-dimensional structure of IWs can be obtained with model predicted amplitudes and satellite-observed PP distances with the KdV-type solutions. The underwater topography is also presented.

Fig. 9. Amplitude distributions (upper panel) of IWs estimated from satellite images using the TLIAR model in the Andaman Sea and corresponding histograms (lower panel).

Fig. 10. The TLIAR model performance for PP distance input errors.

Fig. 11. Observation of IWs in the Andaman Sea using MODIS images (a) acquired at 06:59 on 27 March 2013 and the corresponding in-situ data (b). The red dot indicates the buoy location.

Fig. 12. MODIS image acquired on 28 August 2014 showing clear IW signatures in the South China Sea. The red symbol indicates the in-situ observation location reported in Xu et al. (2020). The insert map shows the extracted profiles indicated by the red solid line.

Fig. 13. Amplitude distributions (left) of IWs estimated using the TLIAR model in the Sulu Sea. The black box indicates the SS3 station in Apel et al. (1985). The right panel shows the corresponding IW amplitude histograms in the black box.